scientific reports

Check for updates

OPEN

Alteration of actin cytoskeletal organisation in fetal akinesia deformation sequence

Ramona Jühlen[1,2,5]✉, Lukas Grauer[2], Valérie Martinelli[1,4], Chantal Rencurel[3] & Birthe Fahrenkrog[1,3,5]✉

Fetal akinesia deformation sequence (FADS) represents the severest form of congenital myasthenic syndrome (CMS), a diverse group of inherited disorders characterised by impaired neuromuscular transmission. Most CMS originate from defects in the muscle nicotinic acetylcholine receptor, but the underlying molecular pathogenesis is only poorly understood. Here we show that RNAi-mediated silencing of FADS-related proteins rapsyn and NUP88 in foetal fibroblasts alters organisation of the actin cytoskeleton. We show that fibroblasts from two independent FADS individuals have enhanced and shorter actin stress fibre bundles, alongside with an increased number and size of focal adhesions, with an otherwise normal overall connectivity and integrity of the actin-myosin cytoskeleton network. By proximity ligation assays and bimolecular fluorescence complementation, we show that rapsyn and NUP88 localise nearby adhesion plaques and that they interact with the focal adhesion protein paxillin. Based on these findings we propose that a respective deficiency in rapsyn and NUP88 in FADS alters the regulation of actin dynamics at focal adhesions, and thereby may also plausibly dictate myofibril contraction in skeletal muscle of FADS individuals.

Congenital myasthenic syndromes (CMS) are neuromuscular disorders that primarily affect the neuromuscular junction (NMJ)[1,2]. The NMJ is a cholinergic synapse by which motor neurons control muscle contraction. Muscle contraction is stimulated by the release of neurotransmitter acetylcholine (ACh) from motor neurons and its binding to the acetylcholine receptor (AChR) at the postjunctional muscle membrane[3]. For stable NMJ formation, AChRs need to cluster and this is regulated by two scaffold proteins: MuSK, a muscle-specific receptor tyrosine kinase, and rapsyn (receptor-associated protein at the synapse). MuSK is activated by binding of agrin, a heparan sulphate proteoglycan, to Lpr4 (low-density lipoprotein receptor-related protein 4), and by binding of DOK7 (downstream of tyrosine kinase 7). Full activation of MuSK results in activation of rapsyn, an increase in rapsyn's concentration at the NMJ, and in consequence in clustering of AChRs[2]. Biallelic mutations in the genes coding for MuSK, rapsyn, and DOK7 cause CMS, in particular fetal akinesia deformation sequence (FADS), the severest form of CMS[4–9]. FADS is an aetiologically heterogenous condition which is distinguished by the inability of affected foetuses to initiate movement in utero[10,11]. For those affected, the lack of foetal movement is responsible for distinct developmental defects, including joint contractures and lung hypoplasia. FADS foetuses are predominantly premature or stillborn, and live-births have a high mortality rate due to respiratory failure.

Beyond the MuSK-DOK7-rapsyn signalling axis, biallelic mutations in the gene coding for nucleoporin 88 (NUP88) were recently identified as cause for FADS[12]. Loss of NUP88 function resulted in defects in AChR maturation in zebrafish and reduced expression of rapsyn[12]. In accordance with the notion that signalling downstream of MuSK and rapsyn involves interactions with the cytoskeleton, we recently reported that depletion of rapsyn and NUP88 perturbed the microtubule network. This perturbation led to defective primary cilium formation and impaired ciliogenesis[13]. The defects in ciliogenesis may account for the pleiotropic developmental defects seen in FADS, but are likely not the sole basis for defective AChR clustering. Clustering of AChRs, however, is orchestrated by the actin cytoskeleton and by actin dynamics[14–19]. Here, we provide evidence that fibroblasts from FADS individuals are characterised by multiple alterations in actin cytoskeleton organisation, including enhanced actin-myosin bundling, enlarged size and number of focal adhesions, and elevated levels of RhoA.

[1]Laboratory Biology of the Cell Nucleus, Institute of Molecular Biology and Medicine, Université Libre de Bruxelles, 6041 Gosselies, Belgium. [2]Institute of Biochemistry and Molecular Cell Biology, Medical School, RWTH Aachen University, 52074 Aachen, Germany. [3]Biozentrum, University of Basel, 4056 Basel, Switzerland. [4]Present address: Laboratory of Neurovascular Signaling, Institute of Molecular Biology and Medicine, Université Libre de Bruxelles, 6041 Gosselies, Belgium. [5]These authors contributed equally: Ramona Jühlen and Birthe Fahrenkrog. ✉email: rjuehlen@ukaachen.de; birthe.fahrenkrog@unibas.ch

We show that the FADS-related proteins rapsyn and NUP88 interact with the focal adhesion protein paxillin at adhesions plaques and that FADS-related mutations in rapsyn and NUP88 disturb this interaction. In light of our results, we propose that dysregulation of the actin cytoskeleton due to the loss of regulatory function of FADS-related proteins at focal adhesions contributes to FADS pathology.

Results

Rapsyn and NUP88 deficiency coincide with altered actin stress fibre appearance

We have recently shown that the formation of primary cilia was compromised in fibroblasts derived from FADS individuals. Likewise, depletion of the FADS-related proteins rapsyn and NUP88 interfered with primary cilia formation[13]. A cross-talk between ciliogenesis and actin cytoskeleton dynamics is well described[20–23], which prompted us to investigate the effect of FADS-like changes on the actin cytoskeleton. To do so, we first depleted rapsyn or NUP88 from normal human foetal MRC5 fibroblasts by RNA interference. Forty-eight hours after siRNA transfection, the actin cytoskeleton was visualised by fluorophore-labelled phalloidin (phalloidin-Alexa 488) and examined by confocal microscopy. We found that actin stress fibres (SFs) appeared reduced upon the respective depletion of rapsyn and NUP88 from MRC5 cells (Fig. 1a). This effect was importantly also evident in primary skin fibroblasts from two FADS individuals, referred to as FADS 1 and FADS 2 (Fig. 1b). FADS 1

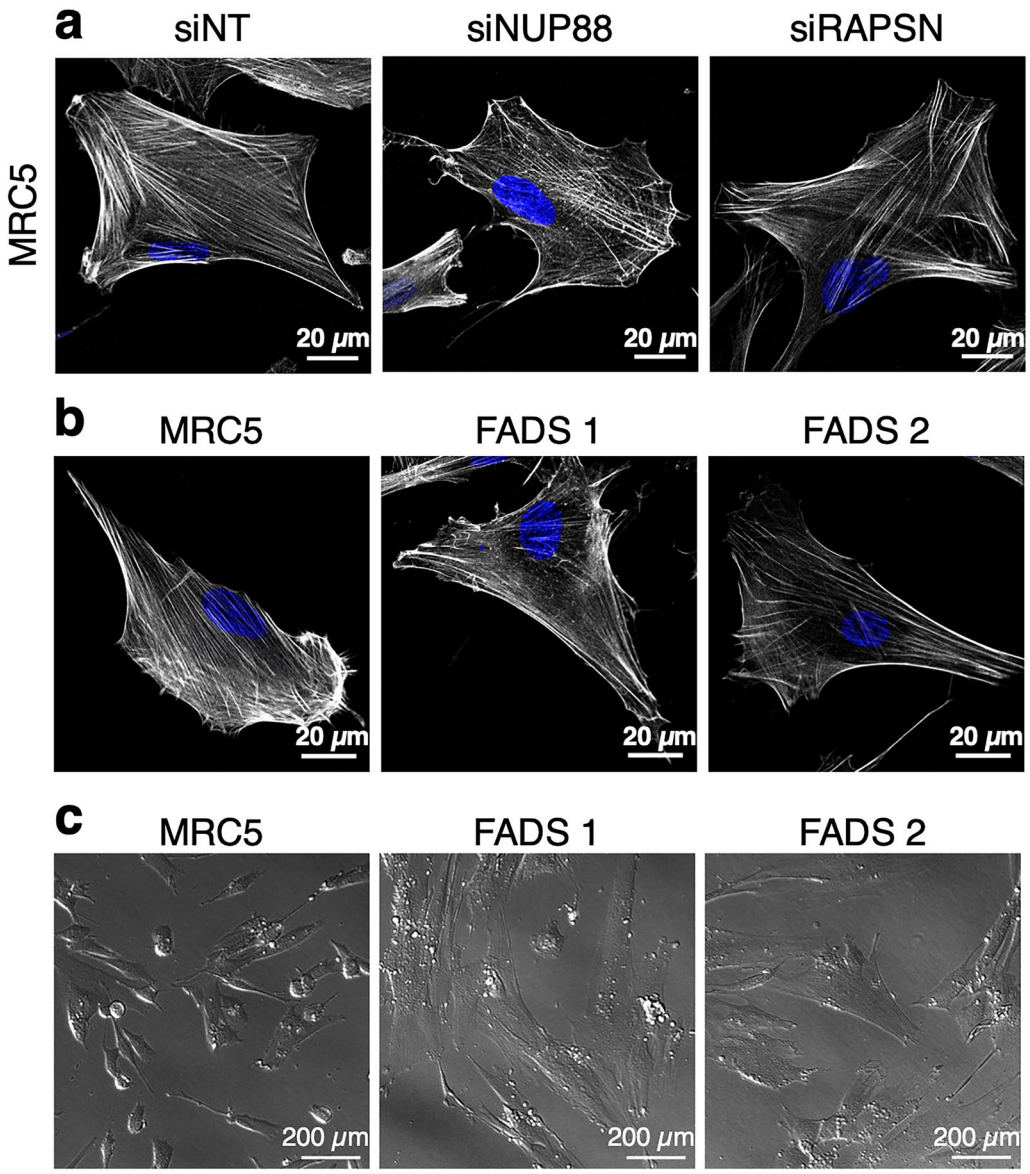

Figure 1. Actin stress fibre formation is perturbed in FADS. Actin stress fibres appeared reduced (**a**) in MRC5 cells NUP88- (siNUP88) and rapsyn (siRAPSN)-depleted as compared to cells treated with non-targeting siRNAs (siNT) and (**b**) in fibroblasts derived from two FADS individuals. Cells were stained with phalloidin to visualise F-actin (greyscale) and DAPI to visualise DNA (blue). Shown are representative confocal images. (**c**) Representative transmitted light images of MRC5 and FADS fibroblasts grown on glass coverslips.

fibroblasts were derived from a foetus carrying an unknown mutation (Coriell Institute; ID: GM11328) and FADS 2 fibroblasts harbour the missense mutation p.E162K in *RAPSN*[4,13]. Consistent with alterations in actin SFs, FADS 1 and FADS 2 fibroblasts exhibited a more elevated and polygonal shaped morphology, as compared to the flat, elongated and spindle-like shaped MRC5 control fibroblasts (Fig. 1c).

Altered cytoskeletal organisation and increased actin-myosin bundling in FADS fibroblasts

To analyse the differences in the actin cytoskeleton in a more quantitative way, we next took advantage of crossbow-shaped surface micropatterns. Such adhesive surface micropatterns induce a controlled polarity of the cytoskeleton due to which cell shape and morphology become normalised[24]. The actin cytoskeleton is very dynamic and can organise itself distinctively (Fig. 2a): branched actin characterises lamellipodia at the leading edge of the cell, parallel non-contractile actin bundles are found in dorsal SFs, whereas anti-parallel contractile actin-myosin bundles form transverse actin arcs and ventral SFs. Dorsal and ventral SFs connect to focal adhesions (FAs), which attach the extracellular matrix to the cytoskeleton via integrins, and are mainly anchored to the actin cytoskeleton by different mechano-sensing linkers, such as vinculin[25–27]. When grown on crossbow-shaped micropatterns, cells typically exhibit a stereotypic organisation of the actin cytoskeleton: lamellipodia appear at the curved leading edge of the cell, dorsal SFs are perpendicular to the leading edge and attach to transverse arcs that line the leading edge. Ventral SFs flank the centre of the crossbow at the trailing edge (Fig. 2a)[28,29]. To particularise the organisation of the actin cytoskeleton in FADS fibroblasts, we first visualised actin SFs by phalloidin and contractile actin-myosin bundles using an antibody to non-muscle myosin II A (NMIIA). Their respective distribution was analysed automated using an ImageJ plug-in and results were illustrated by a colour-coded frequency map denoting pixel intensities (Fig. 2b, Supplementary Fig. S1 online). We found that contractile transverse arcs and ventral SFs were augmented, whereas non-contractile dorsal SFs were reduced in FADS fibroblasts (Fig. 2a, b). Transverse arcs and ventral SFs are characterised by actin-myosin bundling promoted by α-actinin, which cross-links F-actin and is especially abundant on SFs[30]. Consistently, the distribution of α-actinin resembled the phalloidin and NMIIA staining patterns (Fig. 2b). The increase in actin-myosin bundles in FADS cells was not due to changes in the frequency of NMIIA peaks (Supplementary Fig. S2a, b online). Moreover, the overall orientation of actin filaments within the cell (Fig. 2c, phalloidin), as well as the number of actin branches and junctions (Supplementary Fig. S2c, d online), remained unaltered in FADS cells, indicating that the overall connectivity and integrity of the actin network did not change.

To further quantify the changes in actin organisation in FADS cells, we employed the FilamentSensor tool, which allows to define location, orientation, length, and width of single filaments[31]. We found that the overall number of actin filaments was reduced in FADS fibroblasts (Fig. 2d), that actin filaments were shifted towards the curved leading edge of the cell (Fig. 2e), and that actin filaments were generally thicker and shorter in FADS cells (Fig. 2f, g). Together this suggests that an increased actin-myosin bundling results in a gain of thicker actin filaments and in turn a reduction in the overall number of individual actin filaments in FADS fibroblasts.

Distinct rearrangement of focal adhesions in FADS fibroblasts

Given the increase in ventral SFs in FADS fibroblasts, we next examined vinculin, which connects ventral stress fibres to distant FAs[25,27]. Similar to ventral SFs, FAs were likewise increased in FADS cells, both at the leading and the trailing edge of the cell and their orientation within the cell resembled those of the SFs (Fig. 2a–c). Interestingly, while the width of FAs was increased in both FADS fibroblast lines (Fig. 3a), their overall number was only augmented in FADS 2 cells (Fig. 3b). Furthermore, mapping the respective distribution of thick actin filaments and thick (> 2 pixels in width) FAs in FADS cells revealed that thick actin filaments were enriched in transverse actin arcs and ventral SFs (Figs. 2a, 3c), while thick FAs were shifted towards the leading edge of the cell as part of dorsal SFs and to the trailing edge as part of ventral SFs (Figs. 2a, 3c).

FAs promote plasma membrane protrusions at the leading edge of migrating cells by inhibiting the retrograde actin flow and by converting actin-myosin pulling into traction[32]. The described rearrangements of FAs in FADS cells therefore suggest that cell adhesion and/or motility might be impaired. Consistently, FADS cells adhered faster and developed pronounced adhesive FAs and contractile SFs as compared to MRC5 cells (Fig. 3d), when analysed 3 h after seeding. Together these findings suggest that FADS fibroblasts exhibit enhanced forces through FAs and actin-myosin bundles to drive forward movement by membrane protrusions.

Localised myosin contraction in FADS cells is induced by enhanced Rho activation

We have noticed that FADS fibroblasts, when grown on surface micropatterns, developed pronounced plasma membrane blebs at the leading and trailing edge. The bleb cortex stained positive for F-actin (phalloidin), NMIIA, and vinculin (Fig. 4a, arrowheads). The cortex and the interior of membrane blebs were also positive for phosphorylated regulatory light chain of myosin (MLC-P; Fig. 4b, arrowheads), as well as the outer edges of the cell. MLC-P is prerequisite for bundling of contractile SFs and given the enhanced actin-myosin bundling in FADS cells (Fig. 2f, g), we hypothesised that membrane blebbing is a result of an increased intracellular pressure due to altered actin-myosin contraction[33].

Phosphorylation of MLC is mediated by distinct serine/threonine kinases which in turn are regulated by Rho GTPases. In this context, RhoA regulates actin-myosin bundling by activating the ROCK kinase and the formin mDia1[34,35]. By using a GST-pulldown for RhoGTP, we found that the levels of active Rho were increased in FADS cells as compared to control cells (Fig. 4c, left blot). When adding the non-hydrolysable GTP-analogue GTP-γS to the assay to activate Rho, the levels of RhoGTP increased in the control cells and were comparable to those in FADS cells (Fig. 4c, right blot). The increase in active Rho was further supported by wound healing assays. To follow cell migration, the fibroblasts were placed into a culture insert giving rise to a uniform wound of ~ 500 µM, incubated with silicone-rhodamine (SiR)-actin, a cell permeable probe specifically recognising

Figure 2. FADS fibroblasts show localised alterations in actin cytoskeletal organisation and enhanced actin stress fibre bundling. (**a**) Schematic summary depicting typical actin organisation in MRC5 control and in FADS fibroblasts. FADS fibroblasts have augmented contractile transverse arcs and ventral stress fibres. Dorsal stress fibres and focal adhesions are shifted to the leading edge of FADS fibroblasts. (**b**) Colour-coded frequency maps highlight local rearrangements of the actin cytoskeleton in FADS fibroblasts as compared to MRC5 control cells. Cells were grown on crossbow-shaped micropattern and analysed by immunofluorescence microscopy. Images were processed as illustrated in the analysis workflow shown in Supplementary Fig. S1 online. Phalloidin was used to visualise F-actin, non-muscular myosin II A (NMIIA) and α-actinin were used to delineate contractile actin-myosin bundles, and vinculin was used to display mature focal adhesions. The colour-coded map indicates pixel intensities from 0 to 255. (**c**) Orientation of F-actin (phalloidin) and mature focal adhesions (vinculin) in MRC5 and FADS fibroblasts. The respective distribution of F-actin (phalloidin) and vinculin was sampled from images as shown in (b). The circular colour-coded map shows their respective orientation. (**d**–**g**) Quantitative analysis of actin stress fibres using the open-source JRE analysis tool FilamentSensor V1[31]. Shown are violin plots summarising the analysis of: (**d**) actin filament number per cell, (**e**) the distance of actin filaments from the cells' leading edge, as well as (**f**) the width and (**g**) the length of actin filaments. Dunn's non-parametric test was used to calculate pairwise statistics for Kruskal-type ranked data ($p_{\text{Holm-adj.}}$). n denotes the number of observations, black plus single means of biological replicates, and boxplots statistics of biological replicates. Due to the small error size not all statistics of biological replicates are visible underneath the dots.

F-actin, and imaged by time lapse microscopy. We revealed that FADS fibroblasts more efficiently closed the wounds, as compared to MRC5 cells (Fig. 4d–f). Whereas after 25 h almost 100% of the wound area was closed by FADS1 and ~ 80% by FADS2 fibroblasts, only around 40% of the area was closed by MRC5 (Fig. 4d, e). For FADS fibroblasts, loosening of the wound front and migration of individual cells was visible at imaging start, i.e., 5 h after removal of the culture insert (Fig. 4d, t = 5 h, red arrowheads). Consistently, FADS fibroblasts exhibited a significantly increased migration rate/velocity as compared to MRC5 cells (Fig. 4f). Similar results were obtained when performing scratch-wound assays (Supplementary Fig. S3a–c online). Mean area and width of the wounds were comparable at the start of the respective assay (Supplementary Fig. S3d,e online). Our live cell imaging using SiR-actin further confirmed the increase in actin stress fibres (Fig. 4d, t = 29 h) as seen in fixed samples (Fig. 2b, phalloidin). Moreover, MRC5 fibroblasts treated with siRNAs against NUP88 and rapsyn, respectively, more efficiently closed wounds of scratch assays and exhibited an increased migration rate/velocity (Supplementary Fig. S3f–h online). Consistent with the GST-pulldown assays, FADS fibroblasts furthermore had slightly higher levels of MLC-P after wound healing assays (Supplementary Fig. S3i, j online). Together our data indicate that FADS fibroblasts exhibit an increased level of active Rho, which likely directly enhances actin-myosin bundling and contraction. By a sliding mechanism, increased actin-myosin bundling and contraction provokes wider and shorter actin filaments, exactly as described above (Fig. 2f, g).

FADS-related proteins rapsyn and NUP88 are nearby adhesion plaques

To further explore focal adhesions in context of FADS, we next performed in situ proximity ligation assays (PLA) in MRC5 and FADS fibroblasts (see Methods)[36]. We analysed the proximity between rapsyn and NUP88, and vinculin. In MRC5 cells, about 10 foci per cell were detected for vinculin:rapsyn (Fig. 5a, b) and about 15 per cell for vinculin:NUP88 (Fig. 5c, d). In FADS 1 cells, the number of foci increased significantly for both vinculin:rapsyn (about 50 foci per cell) as well as vinculin:NUP88 (about 110 foci per cell) and likewise in FADS 2 cells for vinculin:NUP88 (about 50 foci per cell). The number of PLA foci for vinculin:rapsyn in contrast was reduced in FADS 2 fibroblasts (about 4 foci per cell), likely due to the point mutation in rapsyn in these cells. PLA results were validated by negative controls (Supplementary Fig. S4 online). Together our data suggest that the association of rapsyn and NUP88 with vinculin is perturbed in FADS cells.

For further assessment of rapsyn and NUP88 association with focal adhesions, we exploited the bimolecular fluorescence complementation (BiFC) system in HeLa cells. BiFC is based on protein interactions bringing together ectopically expressed N-terminal (V1-(or VN-)) and C-terminal (V2- (or VC-)) fragments of the Venus protein to reconstitute fluorescence, thus allowing direct visualisation of protein interactions in their normal cellular environment[37]. Rapsyn is known to bind to several actin-binding proteins[38–40], hence we tested the system demonstrating that expression of rapsyn-V1 and actin-V2 in HeLa cells resulted in strong fluorescence in the cytoplasm (Fig. 6a; Supplementary Table S1). In contrast, NUP88 paired with actin did not produce a fluorescence signal (Supplementary S5a online). The fluorescence signal arising from the rapsyn:actin pair was used as reference signal for adjustment of the laser intensity on the confocal microscope to allow quantitative analysis of the assays. The FADS-related E162K mutant of rapsyn paired with actin resulted in cytoplasmic fluorescence similar to the wild-type rapsyn:actin (Fig. 6a). Important for the interaction of actin with actin-binding proteins is a hydrophobic cleft between subunit 1 and 3 of actin[41], and mutations affecting this cleft, i.e. actinΔ143-146 (Fig. 6b) and actinΔ346-349 (Supplementary Fig. S5a online) led to a significant decrease in the cytoplasmic fluorescence of the rapsyn:actin pair (Fig. 6b). Mutations that affect actin polymerisation[42] (actin G215D; Fig. 6b) or mutations in residues surrounding the hydrophobic cleft (actin E167A and actin S350A; Supplementary Fig. S5a online) on the other hand did not impair reconstitution of the Venus fluorescence. Thus, we conclude that rapsyn interacts with actin and that the interaction does not depend on the polymerisation status of actin.

To probe the biochemical interaction of rapsyn and NUP88 with FAs, we next expressed rapsyn and NUP88, respectively, paired with vinculin, but which did not result in any fluorescence signal (Supplementary Fig. S5b online). In contrast, pairs of rapsyn and NUP88 with the FA protein paxillin, produced cytoplasmic fluorescent signals (Fig. 6c, d). Rapsyn:paxillin showed the typical FA staining pattern (Fig. 6c), whereas NUP88:paxillin was

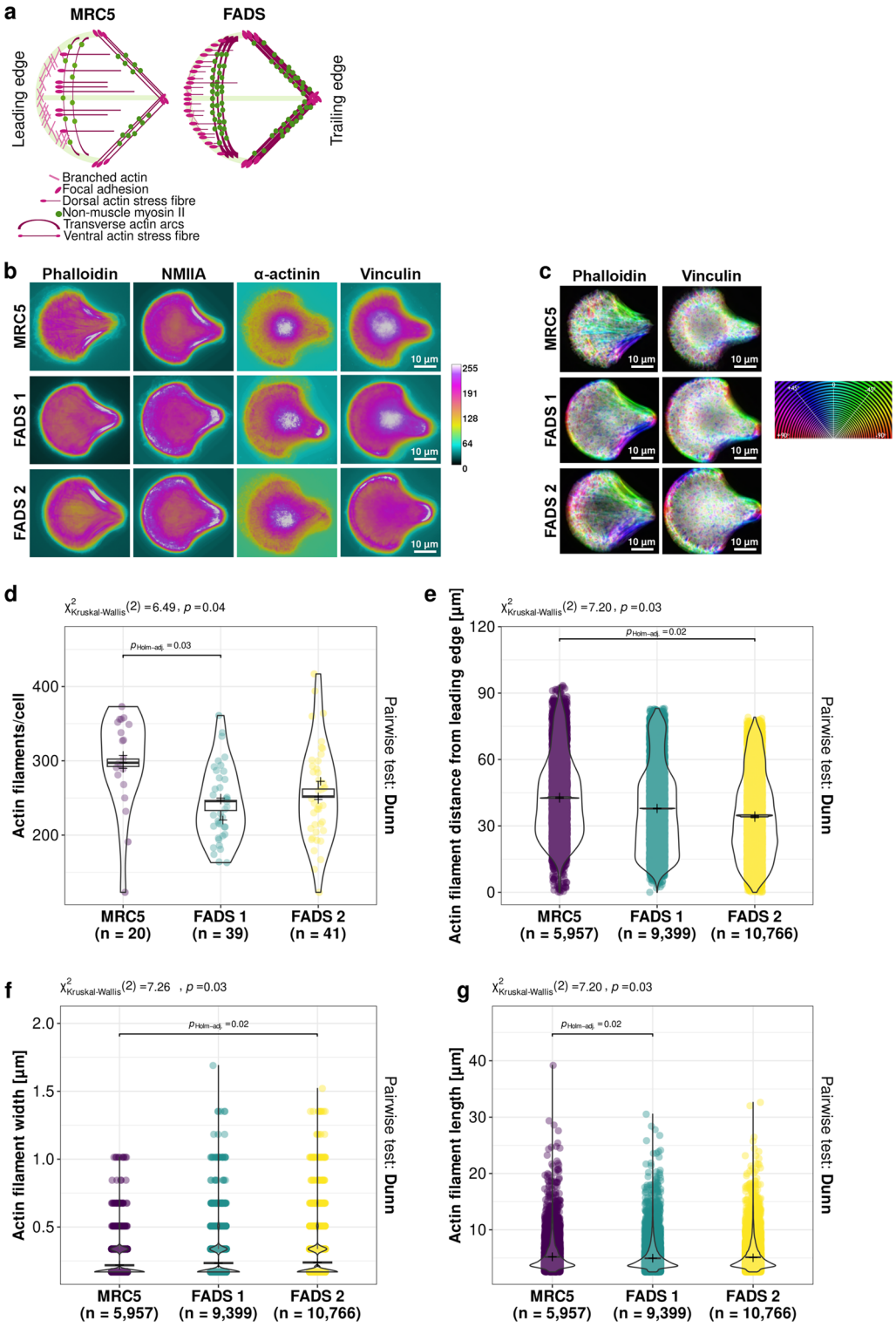
a
MRC5
FADS
Leading edge
Trailing edge
Branched actin
Focal adhesion
Dorsal actin stress fibre
Non-muscle myosin II
Transverse actin arcs
Ventral actin stress fibre
b
Phalloidin
NMIIA
α-actinin
Vinculin
MRC5
FADS 1
FADS 2
10 µm
255
191
128
64
0
c
Phalloidin
Vinculin
d
$\chi^2_{Kruskal\text{-}Wallis}(2) = 6.49$, $p = 0.04$
$p_{Holm\text{-}adj.} = 0.03$
Actin filaments/cell
Pairwise test: Dunn
MRC5 (n = 20)
FADS 1 (n = 39)
FADS 2 (n = 41)
e
$\chi^2_{Kruskal\text{-}Wallis}(2) = 7.20$, $p = 0.03$
$p_{Holm\text{-}adj.} = 0.02$
Actin filament distance from leading edge [µm]
Pairwise test: Dunn
MRC5 (n = 5,957)
FADS 1 (n = 9,399)
FADS 2 (n = 10,766)
f
$\chi^2_{Kruskal\text{-}Wallis}(2) = 7.26$, $p = 0.03$
$p_{Holm\text{-}adj.} = 0.02$
Actin filament width [µm]
Pairwise test: Dunn
MRC5 (n = 5,957)
FADS 1 (n = 9,399)
FADS 2 (n = 10,766)
g
$\chi^2_{Kruskal\text{-}Wallis}(2) = 7.20$, $p = 0.03$
$p_{Holm\text{-}adj.} = 0.02$
Actin filament length [µm]
Pairwise test: Dunn
MRC5 (n = 5,957)
FADS 1 (n = 9,399)
FADS 2 (n = 10,766)

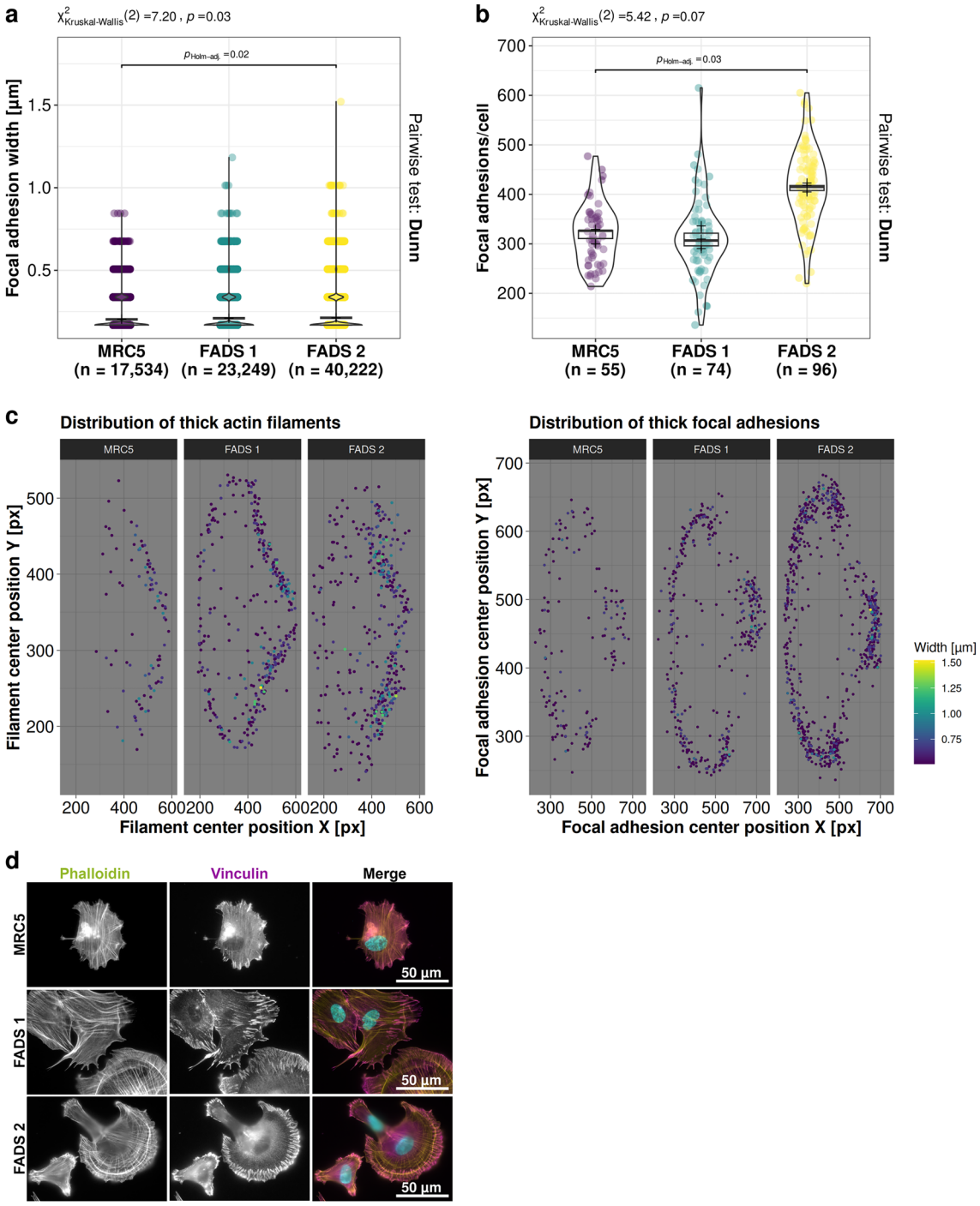

Figure 3. FADS fibroblasts have altered focal adhesion and spreading properties. (**a**, **b**) Quantitative analysis of focal adhesions in MRC5 and FADS fibroblast grown on crossbow-shaped micropatterns using FilamentSensor V1[31]. Shown are violin plots summarising the analysis of: (**a**) the width of focal adhesions and (**b**) their number per cell. Dunn's non-parametric test was used to calculate pairwise statistics for Kruskal-type ranked data ($p_{Holm\text{-}adj.}$). n denotes the number of observations, black plus single means of biological replicates, and boxplots statistics of biological replicates. Due to the small error size not all statistics of biological replicates are visible underneath the dots. (**c**) Colour map representations of the localisation of thick (> 2 pixel in width) actin filaments (left) and thick focal adhesions (right) in MRC5 and FADS fibroblasts. The x-axis indicates the X-coordinate of the filament or adhesion centre and the y-axis the Y-coordinate of the filament or adhesion centre within the crossbow-shaped micropattern. The colour map resembles the filament or adhesion width in µm. Thick actin filaments and thick focal adhesions are mainly found within contractile transverse arcs and ventral stress fibres in FADS fibroblasts (see also Fig. 2a). (**d**) Representative epifluorescence images of fibroblasts imaged 3 h after seeding on crossbow-shaped micropattern. FADS fibroblasts show enhanced spreading immediately after seeding and developed characteristic membrane protrusions. Phalloidin (green) was used to visualise F-actin, vinculin (magenta) to depict mature focal adhesions, and DAPI (blue) to stain DNA.

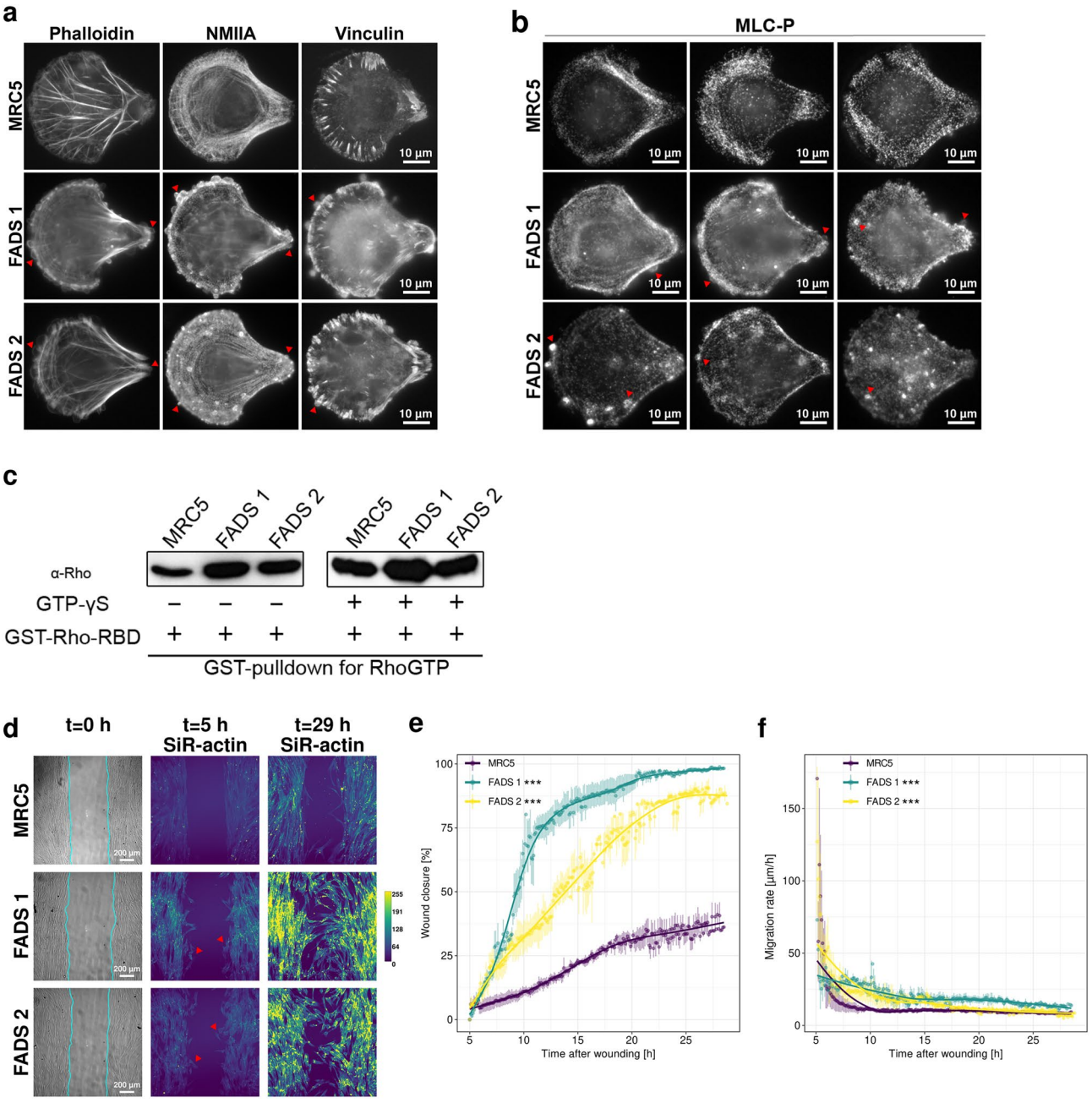

Figure 4. FADS fibroblasts have increased Rho activity and show enhanced cell migration during wound healing assays. Representative epifluorescence images of MRC5 and FADS fibroblasts grown on crossbow-shaped micropattern, (**a**) stained for F-actin (phalloidin), non-muscular myosin II A (NMIIA) and vinculin, as well as (**b**) phosphorylated regulatory light chain of myosin (MLC-P). Membrane blebs at the leading and trailing edge in FADS fibroblast are marked with red arrow heads. Bleb cortex are positive for F-actin, NMIIA and vinculin, whereas bleb interiors are positive for MLC-P. MLC-P staining is enhanced at the edges of FADS fibroblasts. (**c**) GST-pulldown for active Rho revealed that FADS fibroblasts have enhanced RhoGTP levels as compared to MRC5 cells. GTP-γS is a non-hydrolysable GTP-analogue. GST-Rho-RBD, GST-Rhotekin-Rho binding domain. The complete blots are shown in Supplementary Fig. S6a online. (**d**) Wound healing assays in MRC5 and FADS fibroblasts. Live fibroblasts were stained for 1 h with 62.5 nM SiR-actin, 4 h after wounding (removal of a culture insert). Wound closure was monitored every 6 min for 24 h. Shown are representative bright-field (t = 0 h) and SiR-actin time lapse images (t = 5 h and t = 29 h). Original wound area is outlined in turquoise in the bright-field images. Red arrowheads in FADS 1 and FADS 2 indicate early migrating cells at t = 5 h. Grey-values of SiR-actin were adjusted to values in MRC5 to underline over-saturation in FADS fibroblasts (t = 29 h) and are presented as colour-coded Lookup Table. The colour calibration map indicates pixel intensities from 0 to 255. (**e**) Percentage of wound closure and (**f**) cell migration rate (in µm/h) were calculated after image analysis using the ImageJ plugin Wound Healing Size Tool[58]. Dots represent means, vertical lines SEM and curves fitted models of the raw data. At some points errors might be too small to be visible underneath the dots. ***$p < 0.001$. Two-tailed t test was used to calculate statistics.

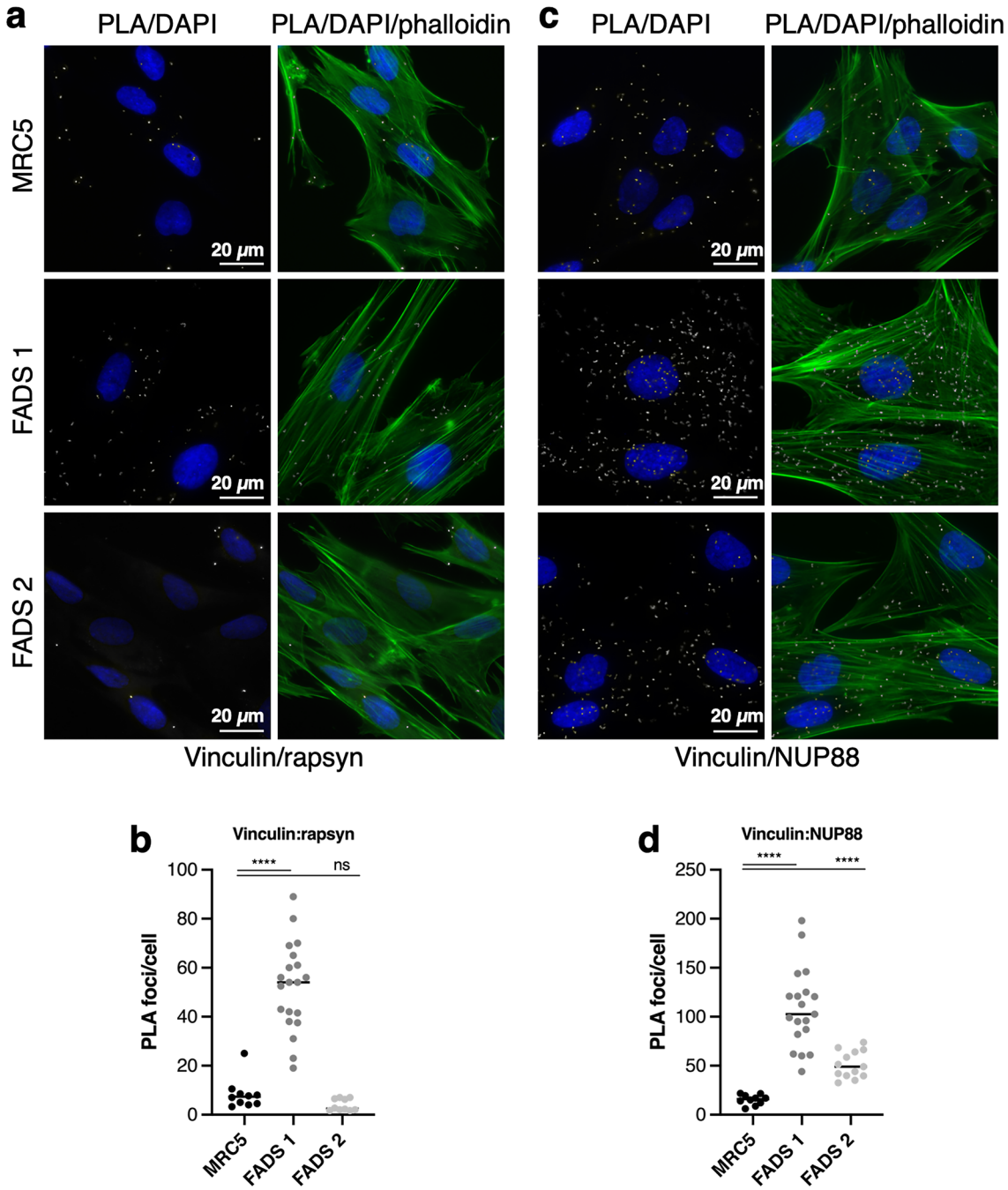

Figure 5. The association of rapsyn and NUP88 with vinculin is altered in FADS fibroblasts. (**a**) Close proximity (about 40 nm) between vinculin and rapsyn was visualised by PLA foci (grey) and (**b**) quantified. Total number of analysed cells: MRC5, n = 21; FADS 1, n = 25; FADS2, n = 36. (**c**) PLA association between vinculin and NUP88 and (**d**) quantification of PLA foci per cell. Total number of analysed cells: MRC5, n = 41; FADS 1, n = 36; FADS 2, n = 60. Phalloidin was used to visualise F-actin (green) and DAPI (blue) for DNA. Shown are representative immunofluorescence images from at least three independent experiments. Black horizontal line represents the median. $^{****}p < 0.0001$; ns, p not significant. Two-Way Anova test was used to calculate statistics.

more homogeneously distributed throughout the cytoplasm (Fig. 6d). FADS-related mutations in both rapsyn (Fig. 6c) and NUP88 (Fig. 6d) consistently led to a significant decrease in the fluorescence signal, suggesting that the interface of rapsyn and NUP88 with paxillin is impaired in FADS.

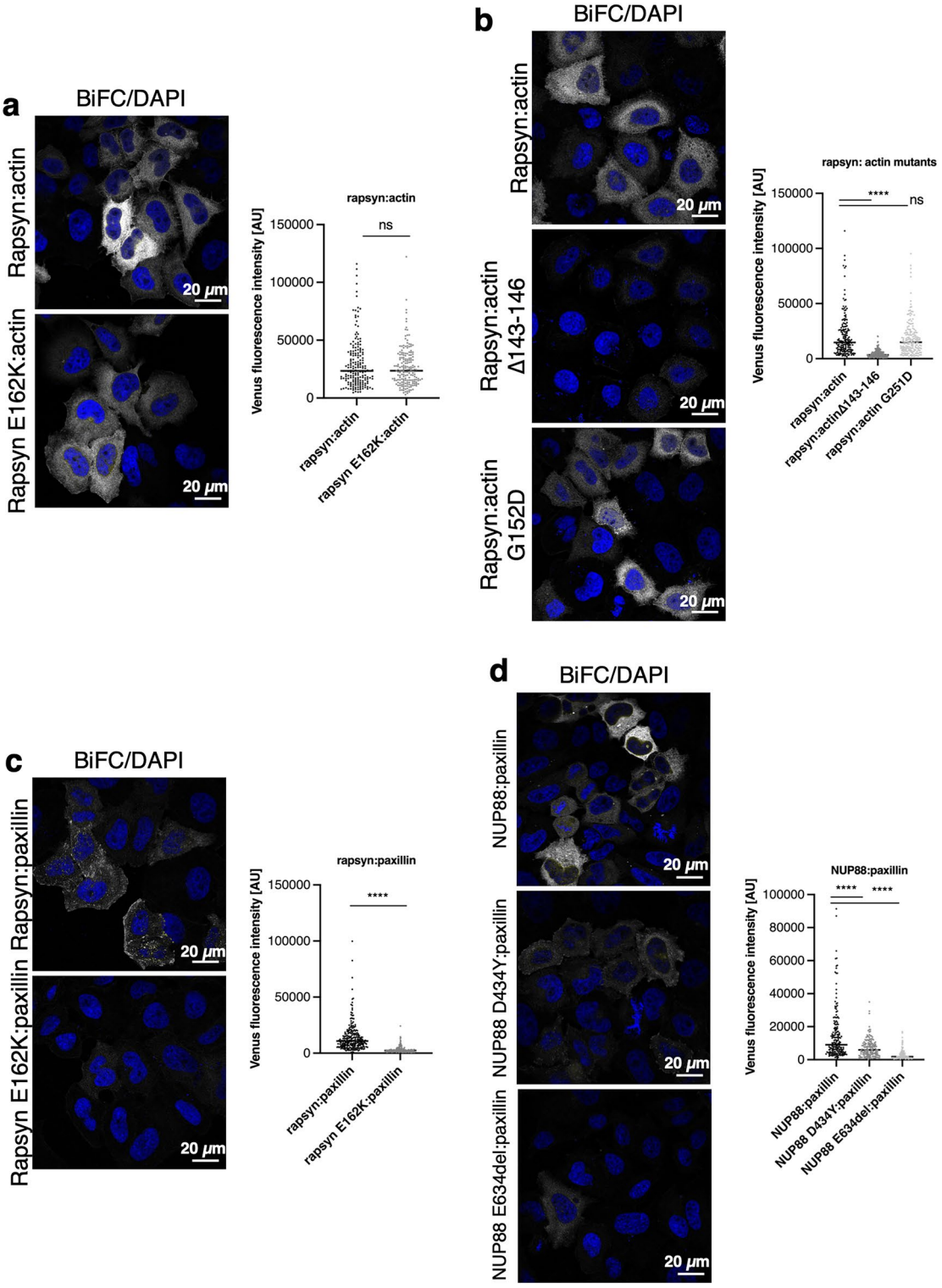

Figure 6. FADS-related mutations in rapsyn and NUP88 abolish their respective interaction with paxillin. Confocal microscopy analysis of BiFC signal produced by interaction between (**a** and **b**) rapsyn and actin, (**c**) rapsyn and paxillin, and (**d**) NUP88 and paxillin in HeLa cells. The FADS-related E162K mutation in rapsyn and the D434Y and E634del mutations in NUP88 largely abolished the interaction of both rapsyn and NUP88 with paxillin. Wild-type and mutant rapsyn further interact with actin and this interaction is disrupted by a mutation in actin's hydrophobic binding cleft (actinΔ143-146), but not by a mutation affecting the polymerisation ability of actin (actinG251D). DNA was stained with DAPI (blue). Shown are representative images from at least three independent experiments. 100–200 transfected cells for each condition were analysed. Black horizontal line represents the median. $^{****}p < 0.0001$; ns, p not significant. Two-Way Anova test was used to calculate statistics.

Discussion

The pathogenesis in fetal akinesia deformations sequence (FADS) has been described extensively and due to modern sequencing approaches several new genes have been linked to the disease[43]. In contrast to the genetic causes, a detailed molecular understanding for the pathogenesis in FADS is still lacking. Here, we use primary fibroblasts from two FADS individuals and we show that these cells have abnormal organisation in the actin cytoskeleton and increased bundling of contractile actin-myosin stress fibres (SFs). We found that the FADS proteins rapsyn and NUP88 localise nearby adhesion plaques by interacting with the focal adhesion protein paxillin and that this interaction is abolished for mutant FADS proteins.

SFs are found in many cultured non-muscle cells and are linked to the plasma membrane by focal adhesions (FAs)[44]. Formation and bundling of SFs is regulated by the small GTPase RhoA, and RhoA is also able to induce FA maturation[45]. Moreover, mature FAs can also provide a positive feedback loop in RhoA activation by serving as enrichment centre for guanine nucleotide exchange factors for RhoGTP[46,47]. Our findings suggest that over-activation of RhoA leads to increased SF formation and FA maturation in FADS fibroblasts; in consequence, we observed that FADS cells have pronounced actin-myosin bundles and mature vinculin-positive FAs. Formation of the neuromuscular junction and AChR development appears primarily supported by non-sarcomeric, sub-membranous actin networks[48], which suggests that the alterations in SF organisation described here may contribute to deficiency in AChR development in FADS individuals. Consistently, we previously found that *nup88*$^{-/-}$ zebrafish had indeed smaller, immature AChR clusters, whereas sarcomeric organisation in zebrafish and affected individuals was largely unaffected[12].

Using proximity ligation assays (PLAs) in control foetal and in FADS fibroblasts we initially mapped rapsyn and NUP88 in proximity to vinculin. Using bimolecular fluorescence complementation (BiFC) in HeLa cells, however, revealed that both rapsyn and NUP88 are not directly interacting with vinculin, but with paxillin. This discrepancy likely arises from the different levels of resolution of the two methods: PLAs permit the detection of protein–protein associations within 40 nm distance[49], whereas BiFC necessitates a distance from at least 7 nm[50]. Our findings confirm recent proximity-dependent biotinylation studies which identified the association of NUP88 with vinculin and paxillin[51]. Paxillin is among the first proteins recruited to newly assembled FAs[52] and it has the largest number of potential protein binding partners within FAs[53]. Phosphorylation of paxillin by the focal adhesion kinase is a key step during FA formation. This is because it creates binding sites that serve as main binding platforms for paxillin interactors[54] and which further promote downstream regulation of actin by FAs. Introducing FADS-related mutations into rapsyn (E162K) and NUP88 (D434Y and E634del) abolished the interaction of either with paxillin. Similar results were obtained in PLAs of vinculin and rapsyn in FADS cells carrying a homozygous E162K mutation in rapsyn. Our results suggest that the loss of the interaction of rapsyn and NUP88 with paxillin (1) leads to a disruption of a regulatory cascade at FAs and (2) gives rise to the actin cytoskeletal anomalies seen in FADS fibroblasts. Actin-myosin contraction regulates focal adhesion maturation and recruitment of core focal adhesion proteins[55]. Therefore, future work shall address how FADS-related proteins regulate actin dynamics at FAs and which key regulatory mechanisms are involved.

Additionally, using BiFC we show that rapsyn interacts with actin possibly through the hydrophobic binding pocket of actin. FADS-related mutation E162K in rapsyn had no influence on the interaction, which can be explained by the fact that rapsyn interacts with actin-binding proteins[39,40] and that these interfaces might rather be affected by the mutation in rapsyn. We therefore hypothesize that a secondary mechanism for rapsyn is in place regulating actin-myosin contraction. This mechanism might further be influenced by the interaction between rapsyn and NUP88, which is abolished in FADS 2 fibroblasts[13]. However, FADS-related mutations in NUP88 appear to have no influence on the interaction with rapsyn (Supplementary Fig. S5c online), indicating that a complex interplay of the rapsyn and NUP88 with the action cytoskeleton. Conclusively, our work establishes actin cytoskeletal anomalies as a key mechanistic factor in FADS fibroblasts possibly caused by perturbed signalling at adhesion plaques. Further investigations how these findings translate into skeletal muscle tissue organisation are needed.

Methods

All experiments were carried out at room temperature unless otherwise stated. Analyses were performed in duplicate and were all repeated at least three times.

Cell culture and transfection

MRC5 (AG05965-G) and FADS (FADS 1; GM11328) fibroblasts were obtained from Coriell (Human Genetic Cell Repository; Coriell Institute, Hamden, NJ, USA). FADS 2 fibroblasts were from an individual harbouring a homozygous c.484G>A (p.Glu162Lys) variant in the *RAPSN* gene (NM_005055.5) as described previously[4]. MRC5 and FADS 2 fibroblasts were grown in Minimum Essential Medium (MEM) medium (Life Technologies Gibco, Gent, Belgium) supplemented with 10% foetal bovine serum (FBS) and 1% penicillin/streptomycin (pen/strep). FADS 1 cells were grown in MEM Alpha (Lonza, Basel, Switzerland) supplemented with 15% FBS and 1% pen/strep. HeLa cells were grown in Dulbecco's modified Eagle medium (DMEM) supplemented with 10% FBS and 1% pen/strep. All cell lines were grown at 37 °C in a humidified incubator with 5% CO_2 atmosphere.

Plasmids were transfected using TurboFect transfection reagent (ThermoFisher Scientific, Basel, Switzerland) and siRNAs using Lipofectamine RNAiMax (ThermoFisher Scientific) following the instructions of the manufacturers. siRNAs were from Dharmacon (Lafayette, CO, USA): *RAPSN* (L-006550-00), *NUP88* (L-017547-01-0005), and non-targeting siRNAs (D-001810-10).

Plasmids

Plasmids pDEST-ORF-V1 and pDEST-ORF-V2 (Addgene plasmids #73637 and #73638) were a gift of Darren Saunders (The Kinghorn Cancer Institute, Sydney, Australia). Rapsyn-V1 and rapsyn-V2 were generated by Gateway cloning using pDONR223-RAPSN (ABIN5316678; Genomics online; GenBank: BC004196.2), as described in[13]. All other constructs were generated by In-Fusion Cloning (Takara, Saint-Germain-en-Laye, France) following the manufacture's instructions. Mutations were inserted by site-directed mutagenesis using the QuikChange Lightning site-directed mutagenesis kit (Agilent Technologies, CA, USA) following the manufacturer's instructions, deletions were inserted by In-fusion cloning. All constructs were verified by DNA sequencing. Plasmids used in this study are listed in Supplementary Table S1, primers are listed in Supplementary Table S2.

Immunofluorescence

Cells were grown on crossbow-shaped micropatterns (size M; CYTOO Inc., Grenoble, France) or glass coverslips in 6- or 24-well plates, respectively, and fixed with 4% PFA in PBS for 5 min, permeabilised with 0.5% Triton-X 100 in PBS for 5 min and then fixed again. For cell spreading experiments, fibroblasts were seeded on coverslips in 24-well plates and fixed after 3 h. Blocking was performed with 2% BSA/0.1% Triton-X 100 in PBS for 30 min. Cells were incubated with the primary antibody over-night at 4 °C in a humidified chamber, washed three times with 0.1% Triton-X 100 in PBS for 5 min and incubated with the secondary antibodies for 1 h in a humidified chamber, washed again and mounted with a drop of Mowiol-4088 (Sigma-Aldrich, St. Louis, MO, USA) containing DAPI (1 µg/ml; Sigma-Aldrich). Cells were imaged using a Zeiss AxioObserver.Z1 microscope (Zeiss, Oberkochen, Germany) or a Leica TCS SP8 confocal laser scanning microscope (Leica Microsystems, Heerbrugg, Switzerland). Images were recorded using the microscope system software and processed using ImageJ, version 1.54c[56].

The following antibodies were used as primary antibodies: mouse anti-vinculin (1:400; clone hVIN-1, Sigma), rabbit anti-non-muscle myosin heavy chain II-A (NMIIA; 1:1000; PRB-440P-050, Eurogentec, Liege, Belgium), mouse anti-α-actinin (1:800; clone EA53, Sigma), rabbit anti-myosin light chain (phospho S20; MLC-P; 1:400; ab2480, Abcam, Cambridge, UK) and rabbit anti-rapsyn (1:200; NBP1-85537, Novus Biologicals, Abingdon, UK). Phalloidin-Alexa Fluor 488 (1:1000; A12379, Life Technologies Invitrogen) and phalloidin-iFluor 594 (1:1000; ab176757, Abcam) were used to stain F-actin. Secondary antibodies were goat anti-mouse IgG Alexa Fluor 488 and Alexa Fluor 568 as well as goat anti-rabbit IgG Alexa Fluor 488 and Alexa Fluor 568 (1:1000; Life Technologies Invitrogen).

Micropattern analyses

A schematic overview of the micropattern analysis procedure is illustrated in Supplementary Fig. S1 online. First, immunofluorescence images of fibroblasts grown on crossbow-shaped micropatterns were automatically analysed using a macro re-written in ImageJ (based on a macro developed by Centre Commun de Quantimétrie (Lyon, France) and CYTOO Inc.). Briefly, images were filtered (Gaussian blur), threshold was set (Median, Huan dark), and micropatterns were centred. Images with multiple nuclei and mitotic cells were automatically excluded, stacks in each colour channel were aligned using plugins *MultiStackReg* (version 1.45) and *TurboReg* (version 2.0.0). Finally, a reference cell for each colour channel using Z-projection with a Rainbow RGB colour-coded Lookup Table was created (Supplementary Fig. S1, 1–7 online).

Next, actin filament organisation (branches and junctions) as well as actin and focal adhesion orientation was investigated in ImageJ using plugins *Analyze Skeleton* (2D/3D; version 3.3.0) and *OrientationJ Analysis* (version 2.0.4), respectively. Phalloidin and vinculin immunofluorescence images of fibroblasts after filtering and alignment of the stacks were used as input files (Supplementary Fig. S1, 8–9 online). Further, in order to examine actin filament and focal adhesion properties in more detail, we used the open-source JRE analysis tool FilamentSensor (V1)[31]. FilamentSensor detects length, width and location (centre X and Y coordinates in an image-specific coordinate system: the x-axis is the horizontal border and the y-axis is the vertical border of the input image) for each single filament of an image. Phalloidin and vinculin immunofluorescence images of fibroblasts after filtering and alignment of the stacks were used as input files (Supplementary Fig. S1, 10 online). NMIIA organisation was analysed as described[57]. Shortly, in ImageJ a 150 px line scan was drawn across NMIIA immunofluorescence staining in actin arcs (and ventral stress fibres; data not shown) and the fluorescence plot profile was obtained. The NMIIA peak frequency was determined in R (version 3.6.0; RStudio, version 1.2.1335) using package *ggpmisc* (version 0.3.1) and *splus4R* (version 1.2-2). NMIIA immunofluorescence images of fibroblasts after filtering and alignment of the stacks were used as input files (Supplementary Fig. S1, 11 online).

Rho GTPase assay

Active Rho Detection kit (#8820; Cell Signaling Technology/Bioke, Leiden, The Netherlands) was used to determine activation of Rho GTPase in the fibroblasts. Cells were harvested under non-denaturing conditions as described by the manufacturer, and 500 µg of lysate was either subjected to treatment with 0.1 mM GTPγS (positive control) or directly processed for affinity precipitation of GTP-bound Rho. Lysate, glutathione resin and GST-Rhotekin-RBD were incubated for 1 h at 4 °C with gentle rocking. Samples were eluted with 2× reducing sample buffer containing 200 mM dithiothreitol, and incubated for 5 min at 95 °C. The eluates were subsequently loaded on 12% polyacrylamide gels and Western blotting was carried out.

Western blot

Cells were lysed in lysis buffer (10 mM Tris–HCl, pH 7.5, 150 mM NaCl, 0.5 mM EDTA, 0.5% Nonidet-P40, protease-phosphatase inhibitor cocktail tablets) and 30 µg of protein were loaded and separated by sodium dodecyl sulphate–polyacrylamide gel electrophoresis (SDS-PAGE). The proteins were transferred onto a PVDF

membrane (Immobilon-P, Merck Millipore, Massachusetts, USA) and the membranes were blocked with PBS containing 5% non-fat dry milk for 30 min. The membranes were then incubated over-night at 4 °C in blocking solution containing a primary antibody followed by washing with TBS containing 0.1% Tween 20 for 30 min. The membranes were next incubated with secondary antibodies for 1 h, washed 1 h in TBS containing 0.1% Tween 20 and developed. X-ray films were scanned and processed using ImageJ.

The following antibodies were used as primary antibodies: rabbit anti-RhoA (1:667; #8789, Cell Signaling Technology), rabbit anti-GAPDH ((14C10) 1:1000; #2118, Cell Signaling Technology), rabbit anti-non-muscle myosin heavy chain II-A (MHC; 1:1000), rabbit anti-phospho-myosin light chain 2 (Ser19; MLC-P; 1:500; #3671, Cell Signaling Technology), and mouse anti-GAPDH (1:500; sc-32233, Santa Cruz Biotechnology Inc, Heidelberg, Germany). Secondary antibodies were alkaline phosphatase-coupled IgG antibodies (1:10000; Sigma-Aldrich) or horseradish peroxidase-coupled IgG antibodies (1:5000; Merck Millipore, Darmstadt, Germany).

Wound healing assays

For assays using culture inserts, fibroblasts were seeded into Culture-Insert 2 Well (Ibidi, Gräfelfing, Germany) at a concentration of 15×10^3 cells per well and grown until they reached 80% confluence. For scratch-wound assays, fibroblasts were seeded in 8-well µ-slide chambers (Ibidi) at a concentration of 30×10^3 cells per well and grown until they reached 80% confluence. Inserts were removed or cell cultures were scratched with a 10 µl sterile pipette tip. Detached cells were washed away twice with complete medium and cells were incubated for 4 h at 37 °C in a humidified incubator with 5% CO_2 atmosphere. Next, the medium was removed from the wells and SiR-actin staining solution (Spirochrome, Stein am Rhein, Switzerland) was added at a concentration of 62.5 nM diluted in complete medium was added. Cell chambers were then equilibrated for 1 h on a Ti2-E microscope (Nikon, Melville, NY, USA) equipped with a LED light engine SpectraX (Lumecor, Beaverton, OR, USA), a Cy5 filter set, a Plan-Apochromat 10× NA 0.5 objective and environmental control system (Ibidi). NIS-Elements software (Nikon) was used to perform fluorescence multi-position imaging every 6 or 30 min for 24 h and the subsequent conversion to image sequences. For documentation of the wound area at t = 0 h cells were imaged using bright-field. Bright-field and fluorescence images were processed and analysed using ImageJ: scratch area, wound coverage of total area, and average and standard deviation of the scratch width were determined using the plugin *Wound Healing Size Tool*[58]. Fluorescence images are presented with a colour-blind-friendly Lookup Table (*mpl-viridis*). The cell migration rate (in µm/h) and the percentage of wound closure were calculated according to (Eq. 1) and (Eq. 2), respectively[59]:

$$Cell\ migration\ rate\ =\ \frac{W_i - W_f}{t} \tag{1}$$

$$Wound\ closure\ =\ \frac{(A_{t=0} - A_{t=\Delta t})}{A_{t=0}} * 100\% \tag{2}$$

where W_i is the average of the initial wound width, W_f is the average of the final wound width (both in µm) and t is the time span of the assay (in h). Additionally, $A_{t=0}$ is the initial wound area and $A_{t=\Delta t}$ is the wound area after n hours of the initial scratch (in μm^2).

Regression models for cell migration rate and wound closure were fitted in R using package *mgcv* (version 1.9-0) based on generalized additive models (GAM)[60]. Differences in parametric coefficients of models for FADS fibroblasts were compared to MRC5 using two-tailed t tests and a confidence interval 95%.

Proximity ligation assay

Fibroblasts grown on cover slips were fixed with 4% PFA in PBS for 5 min, permeabilised with 0.5% Triton X-100 in PBS for 5 min and then fixed again. Blocking was performed with 2% BSA/0.1% TritonX-100 in PBS for 30 min.

All antibodies used for proximity ligation assay (PLA) were diluted in blocking solution. Antibodies mouse anti-vimentin, rabbit anti-vimentin (1:100), mouse anti-vinculin, mouse anti-NUP88, rabbit anti-NUP88 and rabbit anti-rapsyn were incubated at 4 °C over-night in a humidified chamber. Phalloidin-Alexa Fluor 488 was used to visualise F-actin. Excess antibodies were removed by three washing steps using 0.1% Triton X-100 in PBS for 5 min. PLA was performed using Duolink PLA Fluorescent Detection (red) with anti-mouse PLUS and anti-rabbit MINUS oligonucleotides (Sigma-Aldrich). PLA was performed as described elsewhere[61]. Wash buffers were prepared as follows: wash buffer A (0.01 M Tris, pH 7.4, 0.15 M NaCl, 0.05% Tween 20) and wash buffer B (0.2 M Tris, pH 7.5, 0.1 M NaCl). Cover slips were mounted onto microscope slides with Mowiol-4088 containing DAPI. Cells were imaged using a Zeiss AxioObserver.Z1 microscope. Images were recorded using the microscope system software and processed using ImageJ. PLA foci were counted using a macro written in ImageJ: briefly, parameters, scale and image threshold were set (Median, Gaussian blur, MaxEntropy) and particles (PLA foci) counted.

Bimolecular fluorescence complementation assay

HeLa cells were grown in 24-well plates on cover slips and transfected with 200 ng of each plasmid using Turbofect transfection reagent. After 24 h, cells were fixed in 2% formaldehyde in PBS for 15 min, washed in PBS, permeabilised with 0.2% Triton X-100 in PBS containing 2% bovine serum albumin for 10 min. Blocking was performed with 2% BSA in PBS for 30 min and cells were incubated with phalloidin-iFluor 594 reagent (1:1000; ab176757; Abcam) for 1 h. After three washes in PBS, samples were mounted on glass slides using Mowiol containing 1 µg/ml DAPI and stored at 4 °C until viewed. Cells were viewed using a confocal laser scanning

microscope (Leica TCS SP8, Leica Microsystems, Heerbrugg, Switzerland). Images were recorded using the microscope system software with uniform laser settings for all samples. Fluorescence intensity was measured using the Fiji/Image J. Images were processed using Fiji/Image J and Adobe Photoshop.

Statistics

Plots and statistics were created and calculated using R (version 4.2.3, RStudio 2023.03.0 Build 386) using package *ggplot2* (version 3.4.1) and *ggstatsplot* (version 0.11.0). Kruskal–Wallis ranked data has been performed on averaged values of biological replicates to calculate statistics within three groups. Further, to identify where the stochastic differences occur, pairwise comparison using Dunn's test was used and *p*-values were adjusted for multiple comparison using post hoc analysis by the Holm–Bonferroni method. For all statistical tests the following characteristics are given: $X^2_{\text{Kruskal-Wallis}}$, significance (*p* confidence interval 95%), median (μ_{median}) and number of observations (n).

Alternatively, plots and statistics were established using GraphPad Prism 9 (GraphPad Software, Boston, MA, USA). Two-Way Anova tests were carried out to determine *p*-values.

Image design

Figures were created using Adobe Photoshop (version 12.0), Omnigraffle (Omni Group, Seattle, WA, USA), and Inkscape 1.2. Colour panels were adapted from colorbrewer2.org and from the R package *viridis* (version 0.6.2). Colour-blind correction of RGB images was done in ImageJ using plugin *Colourblind Actionbar*.

Data availability

All data generated or analysed during this work are included in this published article.

Received: 15 June 2023; Accepted: 22 December 2023
Published online: 19 January 2024

References

1. Dowling, J. J., Weihl, C. C. & Spencer, M. J. Molecular and cellular basis of genetically inherited skeletal muscle disorders. *Nat. Rev. Mol. Cell Biol.* **22**, 713–732. https://doi.org/10.1038/s41580-021-00389-z (2021).
2. Engel, A. G., Shen, X. M., Selcen, D. & Sine, S. M. Congenital myasthenic syndromes: Pathogenesis, diagnosis, and treatment. *Lancet Neurol.* **14**, 420–434. https://doi.org/10.1016/S1474-4422(14)70201-7 (2015).
3. Hall, Z. W. & Sanes, J. R. Synaptic structure and development: The neuromuscular junction. *Cell* **72**(Suppl), 99–121. https://doi.org/10.1016/s0092-8674(05)80031-5 (1993).
4. Winters, L. *et al.* Massive parallel sequencing identifies RAPSN and PDHA1 mutations causing fetal akinesia deformation sequence. *Eur. J. Paediatr. Neurol.* **21**, 745–753. https://doi.org/10.1016/j.ejpn.2017.04.641 (2017).
5. Wilbe, M. *et al.* MuSK: A new target for lethal fetal akinesia deformation sequence (FADS). *J. Med. Genet.* **52**, 195–202. https://doi.org/10.1136/jmedgenet-2014-102730 (2015).
6. Michalk, A. *et al.* Acetylcholine receptor pathway mutations explain various fetal akinesia deformation sequence disorders. *Am. J. Hum. Genet.* **82**, 464–476. https://doi.org/10.1016/j.ajhg.2007.11.006 (2008).
7. Tan-Sindhunata, M. B. *et al.* Identification of a Dutch founder mutation in MUSK causing fetal akinesia deformation sequence. *Eur. J. Hum. Genet.* **23**, 1151–1157. https://doi.org/10.1038/ejhg.2014.273 (2015).
8. Vogt, J. *et al.* Mutation analysis of CHRNA1, CHRNB1, CHRND, and RAPSN genes in multiple pterygium syndrome/fetal akinesia patients. *Am. J. Hum. Genet.* **82**, 222–227. https://doi.org/10.1016/j.ajhg.2007.09.016 (2008).
9. Vogt, J. *et al.* Germline mutation in DOK7 associated with fetal akinesia deformation sequence. *J. Med. Genet.* **46**, 338–340. https://doi.org/10.1136/jmg.2008.065425 (2009).
10. Ravenscroft, G. *et al.* Fetal akinesia: Review of the genetics of the neuromuscular causes. *J. Med. Genet.* **48**, 793–801. https://doi.org/10.1136/jmedgenet-2011-100211 (2011).
11. Beecroft, S. J. *et al.* Genetics of neuromuscular fetal akinesia in the genomics era. *J. Med. Genet.* **55**, 505–514. https://doi.org/10.1136/jmedgenet-2018-105266 (2018).
12. Bonnin, E. *et al.* Biallelic mutations in nucleoporin NUP88 cause lethal fetal akinesia deformation sequence. *PLoS Genet.* **14**, e1007845. https://doi.org/10.1371/journal.pgen.1007845 (2018).
13. Juhlen, R., Martinelli, V., Vinci, C., Breckpot, J. & Fahrenkrog, B. Centrosome and ciliary abnormalities in fetal akinesia deformation sequence human fibroblasts. *Sci. Rep.* **10**, 19301. https://doi.org/10.1038/s41598-020-76192-1 (2020).
14. Bloch, R. J. Actin at receptor-rich domains of isolated acetylcholine receptor clusters. *J. Cell Biol.* **102**, 1447–1458. https://doi.org/10.1083/jcb.102.4.1447 (1986).
15. Dai, Z., Luo, X., Xie, H. & Peng, H. B. The actin-driven movement and formation of acetylcholine receptor clusters. *J. Cell Biol.* **150**, 1321–1334. https://doi.org/10.1083/jcb.150.6.1321 (2000).
16. Moransard, M. *et al.* Agrin regulates rapsyn interaction with surface acetylcholine receptors, and this underlies cytoskeletal anchoring and clustering. *J. Biol. Chem.* **278**, 7350–7359. https://doi.org/10.1074/jbc.M210865200 (2003).
17. Wang, J. *et al.* Regulation of acetylcholine receptor clustering by the tumor suppressor APC. *Nat. Neurosci.* **6**, 1017–1018. https://doi.org/10.1038/nn1128 (2003).
18. Weston, C. *et al.* Cooperative regulation by Rac and Rho of agrin-induced acetylcholine receptor clustering in muscle cells. *J. Biol. Chem.* **278**, 6450–6455. https://doi.org/10.1074/jbc.M210249200 (2003).
19. Lee, C. W. *et al.* Regulation of acetylcholine receptor clustering by ADF/cofilin-directed vesicular trafficking. *Nat. Neurosci.* **12**, 848–856. https://doi.org/10.1038/nn.2322 (2009).
20. Kim, J. *et al.* Functional genomic screen for modulators of ciliogenesis and cilium length. *Nature* **464**, 1048–1051. https://doi.org/10.1038/nature08895 (2010).
21. Kim, J. *et al.* Actin remodelling factors control ciliogenesis by regulating YAP/TAZ activity and vesicle trafficking. *Nat. Commun.* **6**, 6781. https://doi.org/10.1038/ncomms7781 (2015).
22. Hernandez-Hernandez, V. *et al.* Bardet-Biedl syndrome proteins control the cilia length through regulation of actin polymerization. *Hum. Mol. Genet.* **22**, 3858–3868. https://doi.org/10.1093/hmg/ddt241 (2013).
23. Drummond, M. L. *et al.* Actin polymerization controls cilia-mediated signaling. *J. Cell Biol.* **217**, 3255–3266. https://doi.org/10.1083/jcb.201703196 (2018).
24. Thery, M. Micropatterning as a tool to decipher cell morphogenesis and functions. *J. Cell Sci.* **123**, 4201–4213. https://doi.org/10.1242/jcs.075150 (2010).

25. Tojkander, S., Gateva, G. & Lappalainen, P. Actin stress fibers–assembly, dynamics and biological roles. *J. Cell Sci.* **125**, 1855–1864. https://doi.org/10.1242/jcs.098087 (2012).
26. Seetharaman, S. & Etienne-Manneville, S. Microtubules at focal adhesions—a double-edged sword. *J. Cell Sci.* **2019**, 132. https://doi.org/10.1242/jcs.232843 (2019).
27. Blanchoin, L., Boujemaa-Paterski, R., Sykes, C. & Plastino, J. Actin dynamics, architecture, and mechanics in cell motility. *Physiol. Rev.* **94**, 235–263. https://doi.org/10.1152/physrev.00018.2013 (2014).
28. Jiu, Y. *et al.* Bidirectional interplay between vimentin intermediate filaments and contractile actin stress fibers. *Cell Rep.* **11**, 1511–1518. https://doi.org/10.1016/j.celrep.2015.05.008 (2015).
29. Senger, F. *et al.* Spatial integration of mechanical forces by alpha-actinin establishes actin network symmetry. *J. Cell Sci.* **2019**, 132. https://doi.org/10.1242/jcs.236604 (2019).
30. Crawford, A. W., Michelsen, J. W. & Beckerle, M. C. An interaction between zyxin and alpha-actinin. *J. Cell Biol.* **116**, 1381–1393. https://doi.org/10.1083/jcb.116.6.1381 (1992).
31. Eltzner, B., Wollnik, C., Gottschlich, C., Huckemann, S. & Rehfeldt, F. The filament sensor for near real-time detection of cytoskeletal fiber structures. *PLoS One* **10**, e0126346. https://doi.org/10.1371/journal.pone.0126346 (2015).
32. Chen, T. *et al.* Large-scale curvature sensing by directional actin flow drives cellular migration mode switching. *Nat. Phys.* **15**, 393–402. https://doi.org/10.1038/s41567-018-0383-6 (2019).
33. Paluch, E., Piel, M., Prost, J., Bornens, M. & Sykes, C. Cortical actomyosin breakage triggers shape oscillations in cells and cell fragments. *Biophys. J.* **89**, 724–733. https://doi.org/10.1529/biophysj.105.060590 (2005).
34. Watanabe, N. *et al.* p140mDia, a mammalian homolog of Drosophila diaphanous, is a target protein for Rho small GTPase and is a ligand for profilin. *EMBO J.* **16**, 3044–3056. https://doi.org/10.1093/emboj/16.11.3044 (1997).
35. Leung, T., Chen, X. Q., Manser, E. & Lim, L. The p160 RhoA-binding kinase ROK alpha is a member of a kinase family and is involved in the reorganization of the cytoskeleton. *Mol. Cell Biol.* **16**, 5313–5327. https://doi.org/10.1128/MCB.16.10.5313 (1996).
36. Soderberg, O. *et al.* Direct observation of individual endogenous protein complexes in situ by proximity ligation. *Nat. Methods* **3**, 995–1000. https://doi.org/10.1038/nmeth947 (2006).
37. Kodama, Y. & Hu, C. D. An improved bimolecular fluorescence complementation assay with a high signal-to-noise ratio. *Biotechniques* **49**, 793–805. https://doi.org/10.2144/000113519 (2010).
38. Dobbins, G. C., Zhang, B., Xiong, W. C. & Mei, L. The role of the cytoskeleton in neuromuscular junction formation. *J. Mol. Neurosci.* **30**, 115–118. https://doi.org/10.1385/JMN:30:1:115 (2006).
39. Dobbins, G. C., Luo, S., Yang, Z., Xiong, W. C. & Mei, L. alpha-Actinin interacts with rapsyn in agrin-stimulated AChR clustering. *Mol. Brain* **1**, 18. https://doi.org/10.1186/1756-6606-1-18 (2008).
40. Oury, J. *et al.* MACF1 links Rapsyn to microtubule- and actin-binding proteins to maintain neuromuscular synapses. *J. Cell Biol.* **218**, 1686–1705. https://doi.org/10.1083/jcb.201810023 (2019).
41. Dominguez, R. Actin-binding proteins–a unifying hypothesis. *Trends Biochem. Sci.* **29**, 572–578. https://doi.org/10.1016/j.tibs.2004.09.004 (2004).
42. Blache, U. *et al.* A tumorigenic actin mutant alters fibroblast morphology and multicellular assembly properties. *Cytoskelet. (Hobok.)* **70**, 635–650. https://doi.org/10.1002/cm.21120 (2013).
43. Ravenscroft, G. *et al.* Neurogenetic fetal akinesia and arthrogryposis: Genetics, expanding genotype-phenotypes and functional genomics. *J. Med. Genet.* **58**, 609–618. https://doi.org/10.1136/jmedgenet-2020-106901 (2021).
44. Legerstee, K. & Houtsmuller, A. B. A layered view on focal adhesions. *Biol. Basel* **10**, 11. https://doi.org/10.3390/biology10111189 (2021).
45. Ridley, A. J. & Hall, A. The small GTP-binding protein rho regulates the assembly of focal adhesions and actin stress fibers in response to growth factors. *Cell* **70**, 389–399. https://doi.org/10.1016/0092-8674(92)90163-7 (1992).
46. Iwanicki, M. P. *et al.* FAK, PDZ-RhoGEF and ROCKII cooperate to regulate adhesion movement and trailing-edge retraction in fibroblasts. *J. Cell Sci.* **121**, 895–905. https://doi.org/10.1242/jcs.020941 (2008).
47. Carr, H. S., Morris, C. A., Menon, S., Song, E. H. & Frost, J. A. Rac1 controls the subcellular localization of the Rho guanine nucleotide exchange factor Net1A to regulate focal adhesion formation and cell spreading. *Mol. Cell Biol.* **33**, 622–634. https://doi.org/10.1128/MCB.00980-12 (2013).
48. Mitsui, T. *et al.* Functional association between nicotinic acetylcholine receptor and sarcomeric proteins via actin and desmin filaments. *J. Cell Biochem.* **77**, 584–595. https://doi.org/10.1002/(sici)1097-4644(20000615)77:4%3c584::aid-jcb6%3e3.0.co;2-u (2000).
49. Alam, M. S. Proximity ligation assay (PLA). *Methods Mol. Biol.* **2422**, 191–201. https://doi.org/10.1007/978-1-0716-1948-3_13 (2022).
50. Morell, M. *et al.* Monitoring the interference of protein-protein interactions in vivo by bimolecular fluorescence complementation: The DnaK case. *Proteomics* **8**, 3433–3442. https://doi.org/10.1002/pmic.200700739 (2008).
51. Go, C. D. *et al.* A proximity-dependent biotinylation map of a human cell. *Nature* **595**, 120–124. https://doi.org/10.1038/s41586-021-03592-2 (2021).
52. Kanchanawong, P. *et al.* Nanoscale architecture of integrin-based cell adhesions. *Nature* **468**, 580–584. https://doi.org/10.1038/nature09621 (2010).
53. Zaidel-Bar, R., Itzkovitz, S., Ma'ayan, A., Iyengar, R. & Geiger, B. Functional atlas of the integrin adhesome. *Nat. Cell Biol.* **9**, 858–867. https://doi.org/10.1038/ncb0807-858 (2007).
54. Schaller, M. D. & Parsons, J. T. pp125FAK-dependent tyrosine phosphorylation of paxillin creates a high-affinity binding site for Crk. *Mol. Cell Biol.* **15**, 2635–2645. https://doi.org/10.1128/MCB.15.5.2635 (1995).
55. Schwarz, U. S. & Gardel, M. L. United we stand: Integrating the actin cytoskeleton and cell-matrix adhesions in cellular mechanotransduction. *J. Cell Sci.* **125**, 3051–3060. https://doi.org/10.1242/jcs.093716 (2012).
56. Schindelin, J. *et al.* Fiji: An open-source platform for biological-image analysis. *Nat. Methods* **9**, 676–682. https://doi.org/10.1038/nmeth.2019 (2012).
57. Hu, S. *et al.* Reciprocal regulation of actomyosin organization and contractility in nonmuscle cells by tropomyosins and alpha-actinins. *Mol. Biol. Cell* **30**, 2025–2036. https://doi.org/10.1091/mbc.E19-02-0082 (2019).
58. Suarez-Arnedo, A. *et al.* An image J plugin for the high throughput image analysis of in vitro scratch wound healing assays. *PLoS One* **15**, e0232565. https://doi.org/10.1371/journal.pone.0232565 (2020).
59. Grada, A., Otero-Vinas, M., Prieto-Castrillo, F., Obagi, Z. & Falanga, V. Research techniques made simple: Analysis of collective cell migration using the wound healing assay. *J. Invest. Dermatol.* **137**, e11–e16. https://doi.org/10.1016/j.jid.2016.11.020 (2017).
60. Wood, S. N. *Generalized Additive Models: An Intorduction with R* 2nd edn. (Chapman and Hall/CRC, 2017).
61. Mossaid, I., Chatel, G., Martinelli, V., Vaz, M. & Fahrenkrog, B. Mitotic checkpoint protein Mad1 is required for early Nup153 recruitment to chromatin and nuclear envelope integrity. *J. Cell Sci.* **133**, 456. https://doi.org/10.1242/jcs.249243 (2020).

Acknowledgements

The authors thank Dr. Darren Saunders (The Kinghorn Cancer Institute, Sydney, Australia) for sharing reagents and Antonia van den Broek for technical assistance. The rabbit NUP88-antibody was a kind gift from Dr. Ulrike Kutay (ETH Zurich, Switzerland). Confocal images were acquired at the Imaging Core Facility, Biozentrum,

University of Basel. R.J. was supported by the START-Program of the Faculty of Medicine RWTH Aachen University, by the Habilitation Program of the Faculty of Medicine RWTH Aachen University, and by Fonds of the Chemical Industry. B.F. was supported by a research grant to BF from the Fonds de la Recherche Scientifique-FNRS Belgium (grant numbers J.0102.18), as well as by the Fédération Wallonie-Bruxelles (ARC 4.110. F.000092F). B.F. acknowledges support by the Swiss National Science Foundation/COST (grant IZCOZ0_198146).

Author contributions

Conceptualisation, R.J. and B.F.; methodology, R.J., L.G., V.M., C.R., B.F.; software, formal analyses and writing—original draft preparation, R.J.; writing—review and editing, R.J. and B.F.; supervision, R.J. and B.F.; project administration, R.J. and B.F.; funding acquisition, R.J. and B.F. All authors have read and agreed to the published version of the manuscript.

Funding

Open Access funding enabled and organized by Projekt DEAL.

Competing interests

The authors declare no competing interests.

Additional information

Supplementary Information The online version contains supplementary material available at https://doi.org/10.1038/s41598-023-50615-1.

Correspondence and requests for materials should be addressed to R.J. or B.F.

Reprints and permissions information is available at www.nature.com/reprints.

Publisher's note Springer Nature remains neutral with regard to jurisdictional claims in published maps and institutional affiliations.